12th Deep Sea Offshore Wind R&D Conference, EERA DeepWind'2015

Integrated Modelling Platform for Dynamic Performance Assessment of Floating Wind Turbines

Atsede G. Endegnanew[a]*, Kristian Satertro[b], Sverre Gjerde[c], Harald Svendsen[a], Olimpo Anaya-Lara[d], John O. Tande[a], Kjetil Uhlen[c] and Svein Gjolmesli[b]

[a]*SINTEF Energy Research, Sem Selændes vei 11, Trondheim, Norway*
[b]*FEDEM Technology, Nedre Bakklandet 58C, 7014, Trondheim, Norway*
[c]*Norwegian University of Science and Technology, O. S. Bragstads plass 2E, 7034, Trondheim, Norway*
[d]*Strathclyde University, 6 Richmond Street, Glasgow G1 1XQ. Scotland, United Kingdom*

Abstract

The paper presents an integrated modelling platform that can be used to assess the dynamic performance of an offshore wind turbine mounted on a spar-buoy type floater. Sub-models of generator and converter controllers and the power network are combined with a state-of-the-art numerical simulation of the hydro-, aero- and structural dynamic behavior of the floating wind turbine, using FEDEM Windpower software. The aim is to provide a tool that allows analyzing response of floating turbines to grid faults, interactions and potential conflicts between controllers. A study case of grid disturbance was conducted to illustrate the applicability of an integrated model. A grid fault that lasted 100ms and resulted in 50% residual voltage at the grid connection point was applied, and wind turbine operation both in still water and in large sea wave conditions were analyzed. The results show that the turbine was capable of riding through voltage-dips without severe effects on the electrical or mechanical systems. A significant, but not critical, dip in the tower bending moment was observed. The most affected component of the bending moment is around the axis of the rotor, which is directly related to the loss of generator torque due to the grid disturbance event.

Keywords: Floating turbine; Integrated modelling; Wind turbine modeling; Fault ride through; Motion response; Offshore Wind Introduction

* Corresponding author. Tel.: +47 96833502
  E-mail address: atsede.g.endegnanew@sintef.no

Offshore sites are very promising for the further, large-scale deployment of wind power generation. The reasons are better and more stable wind conditions, more access to new sites, less political controversies, possibilities for larger turbines and improved logistics [1]. Due to the enormous potential, there is substantial political and economic support for offshore wind power around the world. There are already several large offshore wind farms in operation around the world. The turbines in these wind farms are installed in shallow waters with support structures fixed to the seabed. However, a large portion of the potential for harvesting wind energy is found farther offshore, in deeper waters than existing offshore wind farms, and current bottom-fixed technologies are not practical and economical at these sites.

For wind turbines mounted on floating platforms to emerge as viable options, these structures must be reliable in the offshore environment. Additionally, the response to both mechanical and electrical disturbances must be robust. There are many studies focusing on the motion response of floating wind turbines due to environmental loads, such as turbulent wind and waves [2-4]. Regarding the control of floating wind turbines, current research has focused on identifying new control strategies with large emphasis on reduction of platform motions and structural loads [5, 6]. Most proposed controllers have been implemented assuming normal power production and operating conditions, and there has been little mention on how electrical faults in the grid may impact the control performance and overall wind turbine behavior. In [7, 8], a simulation tool dedicated to aero-elastic and structural studies (HAWC2 [9]) has been coupled with a simulation tool dedicated to power system analysis and control design in order to study different electrical and mechanical dynamic phenomena of wind turbines. The impact of grid faults on the mechanical structure of a bottom-fixed DFIG wind turbine was covered.

In this paper, the performance of a floating wind turbine during grid faults is evaluated. The motion response of a floating turbine due to an electrical fault that has occurred in the grid is studied. The simulated wind turbine is a 5 MW synchronous generator with full converter wind turbine mounted on a spar-buoy floater. The generator, converter and the electric power grid are implemented as sub models. These sub-models are combined with a detailed state-of-the-art numerical simulation of the hydro-, aero- and structural dynamic behavior of the floating wind turbine. The study case presented aims to illustrate the applicability of an integrated model to assess the behavior of floating wind turbines and control performance in the event of grid disturbances. The existence of such a tool is essential bearing in mind that advanced controllers concerned with stabilizing the platform fore-and-aft motion rely on the integrity of the torque demand signal (torque control loop), which is highly impacted on during a grid disturbance.

1. Floating wind turbine configuration

At deeper water sites, it might be economical to use floating substructures for wind turbines. However, the technology is at a nascent stage of its development. The consequence of moving towards floating structures is a new set of wind turbine design specifications. These design specifications emerge due to a need to handle the coupled hydrodynamic/aerodynamic forces, as well as the added weight and buoyancy stability requirements. A vast number of permutations of offshore wind turbine platform configurations are possible, considering the variety of available anchors, mooring, floater geometry, and ballast options [10].

In this study, the floating wind turbine is based on the benchmark model developed by the Offshore Code Comparison Collaboration (OC3) [11]. OC3 is an international collaboration established to verify the accuracy and correctness of aero-hydro-servo-elastic codes used for offshore wind turbine simulations. The model used here is a wind turbine installed on a floating spar-buoy support structure, which is an adapted version of the Hywind demo. Hywind is a full scale deep-water floating wind turbine that has been in operation since 2009 [12].

1.1. Wind turbine specification

The wind turbine used is based on the NREL 5MW reference turbine [13] placed on top of the floating spar platform. Key parameters of the wind turbine used in the simulation study are presented in Table 1.

Table 1. Key wind turbine parameters

Parameter	Value
Rated power	5 MW
Number of rotor blades	3
Rotor diameter	126 m
Tower height	77.6 m
Nacelle mass	240 tons
Blade mass	16.84 t
Hub mass	56.84 t
Tower mass	347.46 t
Total weight excluding floating substructure	694.82 t
Shaft axis tilt	5 deg
Blade pre-cone	2.5 deg
Rotor inertia (inc. hub/low speed shaft)	~2.6e7 kgm2

* t = metric tonne (1000 kg).

Additional information and data on the turbine is given in [13] and [14]. The structural damping ratio in percentage of critical damping is set to 1% for the tower and 0.477% for the blades, in accordance with the specifications from the model used in the OC3 project. The global coordinate system, used in the simulation model, has the X-axis pointing towards the direction of the wind, and Z-axis pointing vertically upwards, see Fig. 1.
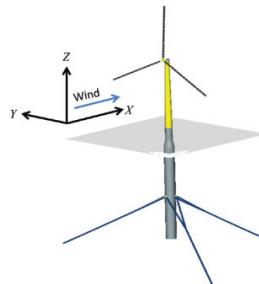

Fig. 1. Global coordinate system for the wind turbine

1.2. Floating spar specification

The floating spar platform is based on the description found in [14]. The equilibrium stick-up position above mean sea-level should be 10 m. To achieve this, the spar mass has been slightly modified, as the mass of the mooring lines will pull it down. This occurs due to the fact that in [14] the mooring lines are modeled as mass-less springs. The platform has a slimmer section at the top where the wave loads are largest, and a larger diameter cross section at the lower part. The two are connected by using a tapered section. The platform is regarded as a rigid body. The mass and inertia are modeled in one point by a point mass and their respective inertias. The buoyancy of the structure is based on the displaced water volume of the submerged part of the platform. The water density is 1025 kg/m^3. Parameters used for the floating substructure are listed in Table 2.

Table 2. Key parameters for the floating substructure

Parameter	Value
Total length of platform	130 m
Elevation of platform above SWL	10 m
Draft below SWL	120 m
Platform diameter above taper	6.5 m
Platform diameter below taper	9.4 m
Top of taper (nominal position below SWL)	4.0 m
Bottom of taper (nominal position below SWL)	12.0 m
CM of spar buoy (nominal position below SWL)	89.9 m
Elevation of mooring line connection (below SWL)	70 m
Mass or spar buoy	7326 t
Platform roll inertia about CM	4.23e9 kg m^2
Platform pitch inertia about CM	4.23e9 kg m^2
Platform yaw inertia about centerline	1.64e8 kg m^2

*SWL = Sea Water Level and CM = Centre of Mass

1.3. Mooring lines

The mooring lines are modeled as structural beam elements with very low bending stiffness and realistic axial stiffness according to data received from Statoil. Each mooring line consists of 106 beam elements, which are subjected to wave loads and drag forces based on the structural response. The specifications of the mooring line data will not be presented due to confidentiality issues.

The mooring lines have a clump weight of about 35 tons attached about 300 m from the spar buoy. This ensures that the mooring lines are always subject to tension and keeps the lower part of the mooring lines from touching the seabed. The mooring line mass and hydrodynamic properties influence on the dynamic behavior of the spar platform. They represent the actual physics of the system as close as possible with the model data available at the time of the work. Fig. 2 (a) shows the complete floating wind turbine with spar buoy and mooring lines, and Fig. 2 (b) shows the delta connections of the mooring lines to the spar buoy.

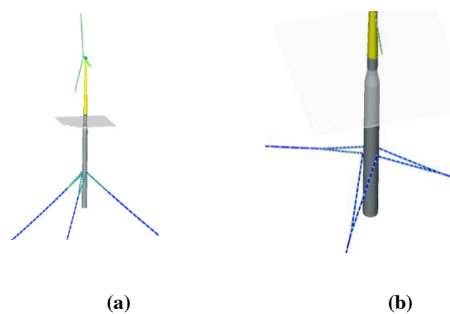**(a)**   **(b)**

Fig. 2. (a) Complete wind turbine with spar buoy and mooring lines, with delta connection and clump weight, (b) Mooring lines shown with delta connection to spar buoy (zoomed in view)

2. Test System Model - turbine, generator, converter and grid

2.1. Electrical system

Fig. 3 illustrates the generator, voltage source converter and electrical grid model used in the simulation model. A full-scale back-to-back frequency converter is placed between a permanent magnet synchronous generator (PMSG) and an electrical grid. The full scale converter consists of a rectifier (generator-side converter), an inverter (grid-side converter) and a DC bus capacitor connected between the two to smoothen the DC link voltage ripple. A chopper circuit is used in the DC link for protection against over voltages. The frequency converter decouples the grid frequency from the generator frequency, and therefore the generator speed. Hence, variable speed operation is possible. Key parameters for the electrical system are given in Table 3.

Fig. 3. Wind turbine generator model with full scale frequency converter interface with the grid

Where:

I_c	Generator side converter output DC-current		$P_{r,loss}$	Generator side converter loss
I_d	Grid side converter input DC-current		$P_{d,loss}$	Grid side converter loss
U_{dc}	DC-link voltage		$P_s + jQ_s$	Input power to the generator side converter
C	DC-link capacitor		$P_c + jQ_c$	Output power of the grid side converter
R_{chp}	Breaking resistor (Chopper)		$i_c \ and \ u_c$	Grid side converter output current & voltage
m_2	Grid side converter modulation index		$R+j\omega L$	Grid impedance
α	Phase angle reference (grid voltage)		u_{grid}	Grid voltage

Table 3. Electrical parameters

Parameter/variable	Value (pu)
DC link capacitance (C)	0.007
DC link chopper resistance (R_{chp})	1.0
Grid resistance (R)	0.01
Grid reactance (ωL)	0.5
Grid voltage	1.0

2.2. Generator speed control

The generator, generator-side converter and their control are modeled simply as a generator speed controller (see the dashed rectangle in Fig. 3). This model simplification was necessary to eliminate the smallest electric time constants, since they are orders of magnitude smaller than the mechanical time constants. Furthermore, with this simplification, complex dynamic equations are avoided, and computational time in the simulation of the integrated system is reduced. This simplified representation of the generator and generator side converter and their control introduces some uncertainty. It is known that a permanent magnet generator would have low damping, and a

sudden change in torque could trigger oscillations. However, it is assumed that any such oscillations are mitigated by control of the generator-side converter.

Fig. 4 shows a block diagram for the generator speed controller. Filtered rotor speed is used to find reference torque from a torque-speed curve (identical to that of a maximum power point tracker control), taken from the NREL 5MW reference turbine [13]. Under the assumption of perfect reference tracking, this reference is equal to the actual generator torque. The measured electrical torque is computed by dividing active power (P_c) by rotor speed. The error between reference and filtered "measured" torques is then fed into a PI regulator. The output of this control block represents the electrical torque developed by the generator (M_e). The de-loading loop is a droop controller used to de-load the generator according to the DC link voltage [15]. De-loading is achieved by multiplying the torque reference by a droop gain that varies as a function of the DC-link voltage. The droop gain is equal to 1 for a DC link voltage below a certain threshold (1.2 pu in the simulations) and the gain linearly decreases to zero when the DC link voltage exceeds the defined threshold. The purpose of this de-loading control is to provide DC-link overvoltage protection support, in addition to the chopper.
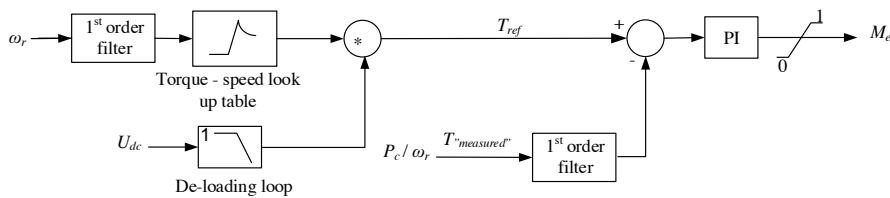
Fig. 4. Block diagram for generator speed controller

2.3. Grid-side converter control

Fig. 5 shows the block diagram for the grid-side converter controller that controls the active power flow into the grid by controlling the DC-link voltage (U_{dc}). The reactive power control is achieved by controlling the converter grid side voltage magnitude $|u_c|$. The references for DC-link voltage (U_{dc_ref}) and reactive power (Q_{c_ref}) are compared with the measured DC-link voltage (U_{dc}) and the estimated reactive power (Q_c), respectively. The errors are then then passed on to PI regulators to give the control variables, i.e. converter output voltage phase angle (α) and grid-side converter modulation index (m_2).
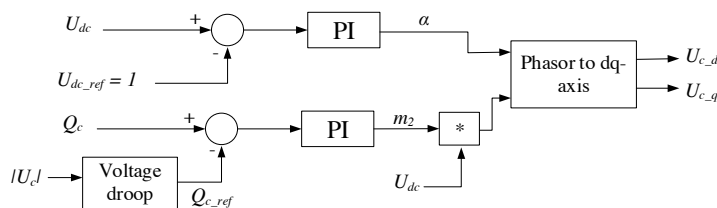
Fig. 5. Block diagram for the grid-side converter controller

The grid-side converter output voltage (d- and q-axis components) is calculated from U_{dc}, α and m_2 using (1) .

$$u_{d\_c} + ju_{q\_c} = m_2 U_{dc} e^{j\alpha} = m_2 U_{dc} \cos\alpha + jm_2 U_{dc} \sin\alpha \qquad (1)$$

For the simulations, a constant U_{dc_ref} =1 pu is used. The reactive power reference, Q_{c_ref}, is generated from a voltage droop function to keep the grid-side converter voltage magnitude $|u_c|$ at constant value of 1 pu. The block

diagram for the voltage droop controller is shown in Fig. 6. The error between the reference and measured $|u_c|$ is fed into a proportional controller.
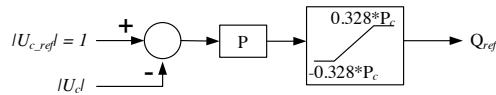

Fig. 6. Block diagram for voltage droop controller

For the reactive power control limits, a power factor of ±0.95 is assumed to be the allowed maximum and minimum power factors at the connection point of the converter to the grid. This ±0.95 power factor limit is a typical requirement set on wind farms by Grid Codes, especially at close-to-rated power production levels [16, 17]. This means that the upper and lower limits of Q_{c_ref} are dependent on the active power produced and are given by:

$$-0.328 P_c \leq Q_{c_{ref}} \leq 0.328 P_c \tag{2}$$

2.4. DC-link dynamics

The DC-link voltage calculation follows Kirchoff's current law. The current flowing out of the generator-side converter is equal to the sum of currents flowing into the DC-link capacitor and the grid-side converter. Including the conditional current in the breaking resistor, this means

$$I_v = I_d + I_c + I_{chp} = I_d + C\frac{dU_{dc}}{dt} + I_{chp} \tag{3}$$

or, re-arranging terms:

$$\frac{dU_{dc}}{dt} = \frac{1}{C} \cdot \left(I_v - I_d - I_{chp}\right) \tag{4}$$

where:

$$I_v = \frac{1}{U_{dc}} \cdot \left(P_s - P_{r,loss}\right) \tag{5}$$

$$I_d = \frac{1}{U_{dc}} \cdot \left(P_c + P_{d,loss}\right) \tag{6}$$

$$I_{chp} = \frac{U_{dc}}{R_{chp}} \tag{7}$$

The total power flowing into the DC-link is equal to the power flowing out plus converter losses. Therefore, the change in DC-link voltage is calculated using (4)–(7). Converter losses are assumed to be zero and during steady-state operations the DC-link voltage is assumed to be constant.

The breaking resistor (chopper) is operating only when the DC-link voltage is above a defined threshold value. Therefore, during normal operation the resistor is disconnected and the current flowing into the resistor, I_{chp}, is zero. This is modelled in the simulation as shown in Fig. 7, using a saturation block to implement the threshold level. Whenever the DC voltage is below the threshold (U_{dc_max}), $1/R_{chp}$ is zero or $R_{chp}=\infty$.
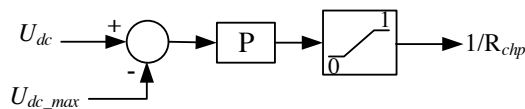

Fig. 7. Breaking resistor (Chopper) model

2.5. Pitch controller

When the turbine reaches its nominal speed, and the generator is producing full torque, the pitch controller is utilized to limit the speed. Physically, this means pitching the blades into the wind, resulting in less power capture. The simulation model of the pitch controller compares measured rotational speed (ω_r) with the maximum allowed rotational speed ($\omega_{r,max}$). The difference is fed into a PI regulator that gives the reference pitch angle (β_{ref}) as an output. A limiter on the PI controller is used to keep $\beta_{ref} = 0$ for $\omega_r < \omega_{r,max}$. Additionally, the pitch controller includes a control loop for active damping of turbine back-and-forth movements in the wind direction. The implementation is according to [18] and the controller's output is denoted as $\Delta\beta$ in the model. Fig. 8 shows the block diagram for the pitch controller.
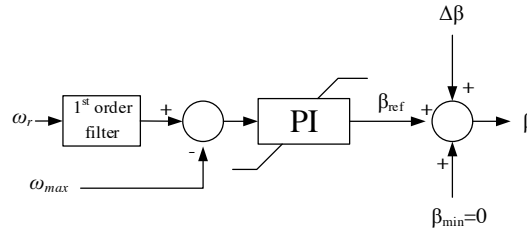
Fig. 8. Block diagram for the pitch controller

2.6. Electrical grid

The electrical grid is modelled as a grid impedance, $R + j\omega L$, connected to a stiff grid with constant voltage, u_{grid}, related to converter voltage and current according to

$$\underline{u}_{grid} = \underline{u}_c - R\underline{i}_c - L\frac{d}{dt}\underline{i}_c \tag{8}$$

where R is the resistance, L is the inductance of the grid connection, and the underlined variables indicate complex quantities in a non-rotating frame. The above equation can be expressed in terms of dq-phasors by using d- and q-axis components $\underline{u}_c = \left(u_d + ju_q\right)e^{j\omega t}$ and $\underline{i}_c = \left(i_d + ji_q\right)e^{j\omega t}$. By inserting the dq-voltage and current expressions into (8) and rearranging, the first-order differential equation of the grid-side converter output currents are given as:

$$\frac{d}{dt}i_{c\_d} = \frac{1}{L}\left(u_{grid\_d} - u_{c\_d} + Ri_{c\_d} + \omega Li_{c\_q}\right)$$
$$\frac{d}{dt}i_{c\_q} = \frac{1}{L}\left(u_{grid\_q} - u_{c\_q} + Ri_{c\_q} - \omega Li_{c\_d}\right) \tag{9}$$

3. Implementation in FEDEM Windpower

FEDEM Windpower is a multi-body simulation software for analyzing dynamic behavior in flexible mechanisms [19]. The software has been available for almost two decades and was initially used mainly for automotive applications. However, in recent years possibilities for including hydrodynamic and aerodynamic loads from wind turbines have been implemented. Regular and irregular wave models and deep and shallow water are supported. The software also incorporates an internal control system editor which is used to build the control system for the floating turbine model. The solver supports the use of Nastran and Sesam mesh models, and utilizes

the Craig-Bampton method with guyan reduction of large element models to reduce computation time. The dynamic equation at time t is given by the balance of system forces as:

$$F_I(t,r,\dot{r},\ddot{r}) + F_D(t,r,\dot{r},\ddot{r}) + F_S(t,r,\dot{r},\ddot{r}) - Q(t,r,\dot{r},\ddot{r}) = 0 \tag{10}$$

Where: r is the position vector for all dimensions of freedoms (DOF) in the system
F_I represents inertia forces
F_D represents damping forces
F_S represents elastic forces
Q represents input loads (forces and torques) and gravitational forces

The dynamic equation is solved using the matrix formulation given in (11). The matrices $\mathbf{M}$, $\mathbf{D}$, $\mathbf{K}$ and vector $\mathbf{Q}$ is updated at each time step.

$$\mathbf{M}\Delta\ddot{r} + \mathbf{D}\Delta\dot{r} + \mathbf{K}\Delta r = \mathbf{Q} \tag{11}$$

Where: $\mathbf{M}$ is the mass matrix
$\mathbf{D}$ is the damping matrix
$\mathbf{K}$ is the stiffness matrix
$\mathbf{Q}$ is the load vector

With fully integrated solving of structural dynamics, hydro and aerodynamic loading, each structural component of the floating wind turbine is represented with a finite element model. The damping matrix is based on the Rayleigh method, using proportionality factors for the mass and the stiffness matrix, α_1 and α_2, respectively. The dynamical equation is integrated using the Newmark time step method combined with Newton-Rhapson iterations. The system matrices are regenerated at each time step. The wind loads are calculated by use of the NREL AeroDyn [20] open source software package. The software's built-in active control system editor and solver allowed creation of electrical system controllers, pitch controller and power system models directly into the modeling environment.

A simulation time step of 0.025s is used as a trade-off between the electrical and mechanical responses, which are orders of magnitude apart. It is assumed that the electric time constants ≈ 0, i.e. all the electrical systems and control loops have immediate response.

The interface between the model of the electrical system and the mechanical model is rotor speed (ω_r) and speed of tower movement ($\Delta\beta$), coming out from the mechanical model of the floating turbine. The electrical torque (M_e) and pitch angle (β) are going into the mechanical part. This interface between the electrical and mechanical sub-components of the floating wind turbine model is illustrated in Fig. 9.
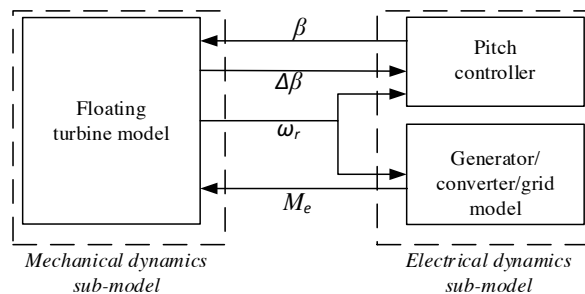

Fig. 9. FEDEM Windpower - floating wind turbine implementation

4. Simulation studies

In order to demonstrate the applicability of the integrated floating wind turbine model, a network disturbance is used to assess its dynamic performance. A constant wind speed of 11 m/s is used, and the turbine is producing 90% of its rated power in a still water with no waves before the fault is applied at t = 80 s. A symmetrical three-phase fault in the grid leads to a voltage dip of 80% at the stiff grid (u_{grid}) in the simulation model. This fault causes the voltage at the connection point between the converter and the grid to drop by 50%. The depth and duration of the voltage disturbance are selected in such a way that the voltage profile lies within the fault ride through requirements found in most Grid Codes[16, 17, 21]. After 100 ms, the grid voltage is immediately restored. Fig. 10 shows the voltage drop caused by the grid fault at the grid and at the converter terminal.
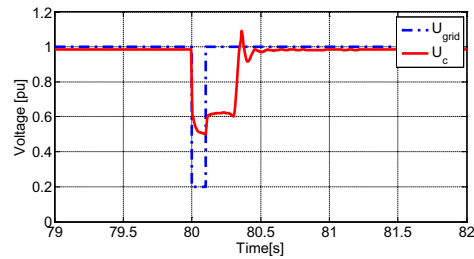
Fig. 10. Grid voltage and converter terminal voltage

The converter terminal voltage does not immediately return to the pre-fault value after fault clearance, but remains low until about 80.3 s. The reason for this is the absence of a current controller which leads to very high grid side currents of nearly 2 pu that compensate for the low voltage, enabling a recovery of active power (see Fig. 11) without a recovery of the voltage. Since voltage is controlled via reactive power reference with limits dependent on active power, this influences the voltage controller in such a way as to hinder immediate voltage recovery. This is an artefact of the simplified modeling of the electrical system that does not affect the conclusions of this study regarding mechanical system response to a grid fault. There is an additional simulation effect around 80.3 seconds in all the curves. This is caused by wind-up of the integrator term in the speed controller PI block with saturation, leading to overshooting response of the control system. This is most clearly seen in Fig. 18(a). The subsequent torque dip after wind-down results in associated dips in the other curves. Again, this is an artefact of the simplified modeling that does not affect the paper's conclusions.

With the above comments in mind, the electrical results show that the turbine is able to ride through the fault and to recover stability once the fault is cleared, and continue producing active and reactive power at same levels as in the pre-fault period. From Fig. 11, it can be seen that during the fault, active power output from the turbine is reduced to less than 0.25 pu while reactive power output is increased to 1.0 pu. Since the grid-side converter is operating in voltage control mode, the reactive power output of the converter is increased to support the terminal voltage of the converter.
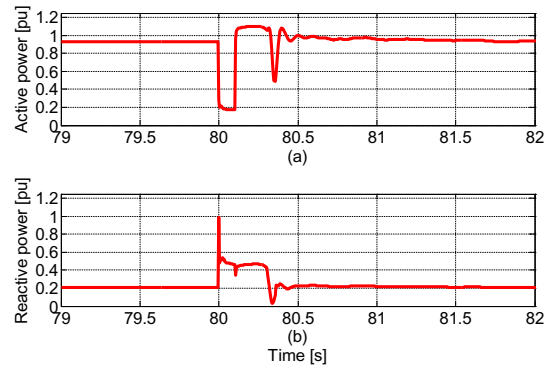
Fig. 11. Active and reactive power output from the grid-side converter

The grid-side converter is prevented from transferring all the active power produced by the generator during the fault. Due to the imbalance between generated and exported power, the DC-link voltage increases rapidly as shown in Fig. 12. The DC-link voltage controller threshold is set to 1.2 pu, and the DC-chopper and de-loading loop are activated after the voltage has passed this threshold. It is evident that the controllers are able to limit the DC-link voltage with the maximum value reaching 1.25 pu.
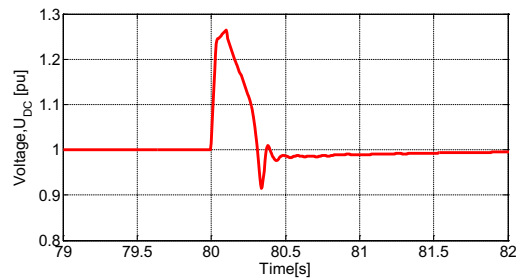
Fig. 12. DC-link voltage

As mentioned earlier, DC-link voltage control using de-loading loop is achieved by reducing the reference electrical torque linearly when the DC-link voltage exceeds the pre-defined value, 1.2 pu in this case. The reduction in electrical torque causes an increase in rotor speed which leads to conversion of aerodynamic input power into kinetic energy, as seen in Fig. 13. Fig. 13(a) shows that the electrical torque is reduced to 0.3 pu during the fault. This is a large and abrupt change in the generator torque, which may impact the controller's performance and overall turbine response (due to the fact that controller's operation uses the torque as input signal). Fig. 13(b) shows the resulting generator speed increase. There is a very small speed increase of 0.8%. Additionally, there is a poorly damped generator speed oscillation with frequency of approximately 2.5 Hz, which is believed to be related to non-optimal torque controller tuning, since the drive train is modelled as a rigid body. The increase in speed is small because of the large moment of inertia of the rotor compared to the duration of the fault. The change in speed is not high enough to activate the pitch controller.
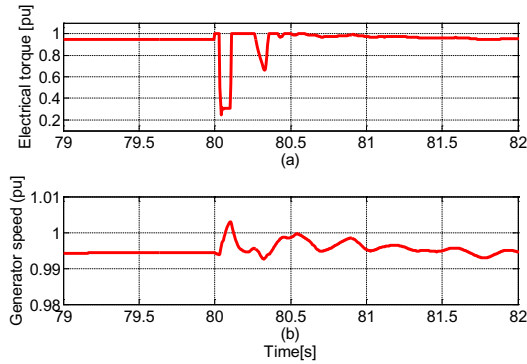
Fig. 13. Rotor shaft torque and generator speed curves

Fig. 14 shows the bending moment at the top of the tower around the global X-, Y- and Z-axis vectors (see Fig. 1 for coordinate system reference) during the grid fault. The bending moment around the X-axis is caused by the generator moment; the bending moment around the Y-axis is caused by the thrust force from the wind; and the bending moment around the Z-axis is the torsional moment or twisting of the tower. The curves in Fig. 14 show that there is a significant reduction in the tower top bending moment around the X-axis, which is in the direction parallel to the wind direction. This is as expected since the electrical torque is directly related to the tower bending moment around the X-axis. The change in bending moment around the Y-axis is unnoticeable. This is also to be expected as the bending moment is related to the thrust from the wind and there is no change in the wind dynamic forces in the simulation study which was run with constant wind speed. The bending moment around the Z-axis, which is the direction in parallel to the tower, increases slightly.
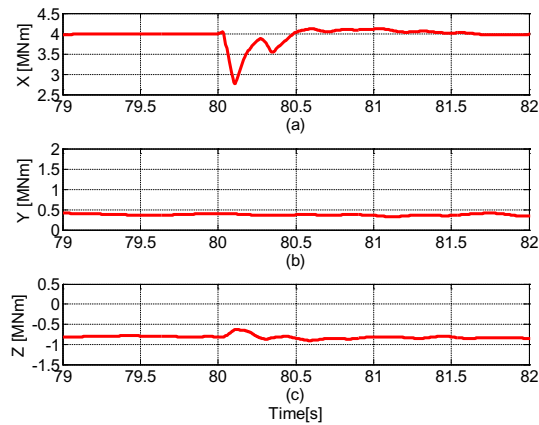

Fig. 14. Tower top bending moment (a) around X-axis (wind direction), (b) around Y-axis, and (c) around Z-axis

Fig. 15 shows the bending moment at the bottom of the tower around the global X-, Y- and Z-axis vectors. Similar to the top bending moments, the tower bending moment around the X- and Z-axis are affected by the fault, while the bending moment around the Y-axis shows no variation due to the disturbance.
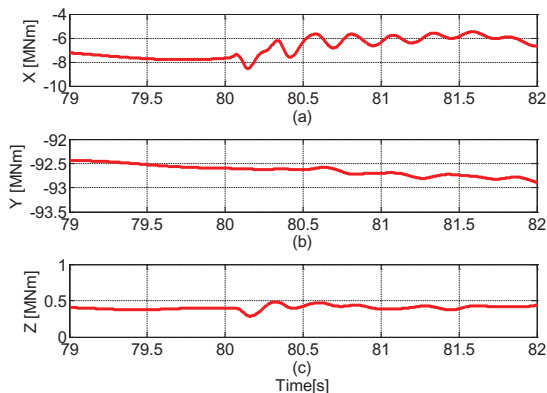
Fig. 15. Tower bottom bending moment (a) around X-axis (wind direction), (b) around Y-axis, and (c) around Z-axis

As a second case, an identical fault scenario is studied with the floating turbine experiencing some sea wave conditions. This case was included to get an indication of how the dynamic loads due to global motions occurring from wave loads affects the tower top bending moment, hence to get an idea of the magnitude of the grid fault relative to the motion induced loads. Sea waves, with significant wave height of 6m and spectra peak period of 11 seconds modelled with Jonswap wave spectra, are included in the simulation. This wave condition is chosen to represent large sea waves, but not so large that they are unlikely to occur.

Fig. 16 shows the tower top bending moments around the X-, Y- and Z-axes for a period of 50 s to show the global motions due to the wave loads. Fig. 16 shows same results but with close up view around the fault incident. The results for the electrical outputs are similar to that of the no wave condition. However, the dip in the bending moment around X- axis is slightly higher. This is because of the slightly different rotor speed between the two scenarios at the fault incident.
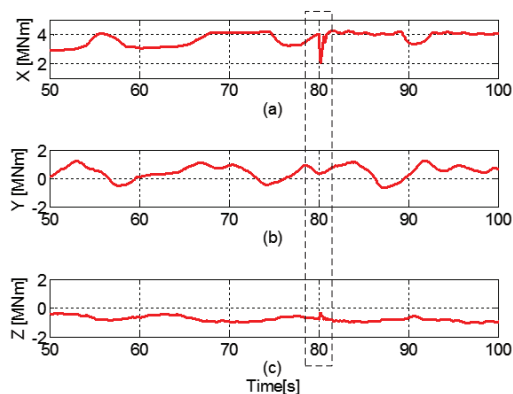

Fig. 16. Tower top bending moment with sea wave conditions (a) around X-axis (wind direction), (b) around Y-axis, and (c) around Z-axis
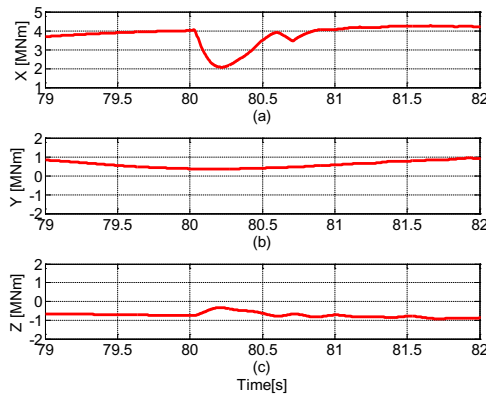
Fig. 17. Tower top bending moments around X-, Y- and Z-axes for floating turbine operating in sea waves (close to the fault occurrence time)

Fig. 18 shows the blade root bending moments of the floating wind turbine. However very small, the moments around Y- and Z-axes are affected by the disturbance while there is no significant change in the bending moment around the X-axis.
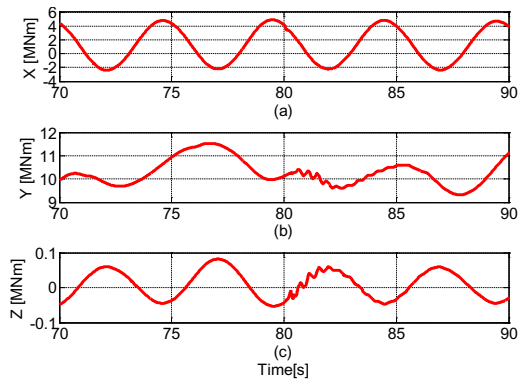

Fig. 18. Blade root bending moments around X-, Y- and Z-axes for floating turbine operating in sea waves

The tower-top bending moment fluctuations observed in these two cases are about 30% and 50%. As aerodynamic load fluctuations of 30% due to turbulence are commonplace, this is believed not to be critical and not a driving factor for turbine design. Note that issues regarding drivetrain oscillations are not included in this analysis as the drivetrain was represented by a single rigid element. The global response/load transfer onto the tower is considered as valid. Further detailing of the drive train will add local dynamics of the shaft and rotor superimposed onto the results obtained.

5. Conclusions

An integrated model platform suitable for detailed analysis of grid and floating wind turbine interactions has been presented and demonstrated. The simulation models used for the mechanical and electrical systems of the floating wind turbine and the grid were described in detail. The floating turbine's response to a symmetrical three phase grid fault, that caused a 50% voltage drop at the turbine converter's terminal, was studied. It was found that

the turbine rides through voltage-dip without severe effects on electrical systems. In the mechanical system, significant, but not critical, dip in tower top bending moment around the X-axis, direction parallel to the wind, was observed. A minor spike was seen on the tower top bending moment around Z-axis while Y-axis bending moment showed no significant change. The level of the stresses caused by the fault was of limited magnitude and did not jeopardize the stability of the turbine structure. It is worth noting, however, that the current results have been obtained by simulations in a particular operating condition for a particular grid fault event. A more thorough analysis should be conducted in order to judge whether mechanical response due to grid faults are in fact design-driving or not. It should also be noted that controller parameters have not been optimized for the present study, and it can therefore be expected that better tuned parameters would improve the performance.

The simulation results presented in this paper may be validated by comparison with measurements from actual fault cases experienced by existing floating turbines, or through a controlled setup using of a short-circuit emulator such as the 8 MVA ETEST facility together with the planned NOWERI 225 kW floating test turbine.

6. References

[1]   A. Henderson, C. Morgan, B. Smith, H. Sorensen, R. Barthelmie, and B. Boesmans, "Offshore Wind Energy in Europe A Review of the State-of-the-Art," *Wind Energy*, vol. 6, pp. 35-52, 2003.

[2]   Y. XiaoRong, Z. Liang, W. HaiTao, and Z. Jing, "Study to motion response of floating offshore wind turbine under the turbulent wind," in *Electrical and Control Engineering (ICECE), 2011 International Conference on*, 2011, pp. 3683-3686.

[3]   S. Gueydon and X. Wei, "Floating wind turbine motion assessment," in *OCEANS 2011*, 2011, pp. 1-10.

[4]   B. Skaare, T. D. Hanson, F. G. Nielsen, R. Yttervik, A. M. Hansen, K. Thomsen*, et al*., "Integrated Dynamic Analysis of Floating Offshore Wind Turbines," in *European Wind Energy Conference and Exhibition*, Milan, Italy, 2007, pp. 7-10.

[5]   J. M. Jonkman, "Influence of control on the pitch damping of a floating wind turbine," presented at the ASME Wind Energy Symposium, Reno, Nevada, 2008.

[6]   H. Namik and K. Stol, "Individual pitch control of floating offshore wind turbines," *Wind Energy*, pp. 74-85, April 2009 2009.

[7]   B. Barahona, A. D. Hansen, N. A. Cutululis, and P. Sørensen, "Coupling of HAWC2 and Matlab: Towards an Integrated Simulation Platform," in *European Wind Energy Conference and Exhibition*, Warsaw, Poland, 2010.

[8]   B. Barahona, P. Sørensen, O. Anaya-Lara, and J. Tande, "Integrated Analysis of DFIG Drive Train and Power Electronics Dynamics during Electrical AC Faults and Wind Distrubances," presented at the EPE Joint Wind Energy and T&D Chapters Seminar, Trondheim, Norway, 2011.

[9]   (04/12/2013). Available: http://www.hawc2.dk/

[10]   S. Butterfield, W. Musial, and J. M. Jonkman, "Engineering challenges for floating offshore wind turbines," presented at the Offshore wind conference, Copenhagen, Denmark, 2005.

[11]   J. M. Jonkman and W. Musial, "Offshore Code Comparison Collaboration (OC3) for IEA Task 23 Offshore Wind Technology and Deployment," NRELDecember 2010 2010.

[12]   Statoil. Available: www.statoil.com

[13]   J. M. Jonkman, S. Butterfield, W. Musial, and G. Scott, "Definition of a 5-MW Reference Wind Turbine for Offshore System Development," NRELFebruary 2009 2009.

[14]   J. M. Jonkman, "Definition of the Floating System for Phase IV of OC3," NRELMay 2010 2010.

[15]   G. Ramtharan, A. Arulampalam, J. B. Ekanayake, F. M. Hughes, and N. Jenkins, "Fault ride through of fully rated converter wind turbines with AC and DC transmission systems," *IET Renewable Power Generation*, vol. 3, pp. 426-438, 2009.

[16]   NGET, "The Grid Code," in *Issue 5, Revision 1*, ed, 2012.

[17]   T. T. GmbH, "Grid Code - High and Extra High Voltage," ed, 2012.

[18]   F. N. Finn Gunnar Nielsen, B. Skaare, J. O. Tande, I. Norheim, and K. Uhlen, "A method for damping tower vibrations in a wind turbine installation," 2012.

[19]   R. D. Blevins, *Flow-Induced Vibrations*, 2nd ed. USA: Krieger Publishing Company, 1990.

[20]   NREL, "Aerodyn," ed: NREL.

[21]   M. Santos-Mugica, E. Robles, A. G. Endegnanew, E. Tedeschi, and J. Giebhardt, "Grid integration and power quality testing of Marine Energy Converters: Research Activities in the MARINET project," presented at the 9th international conference on Ecological Vehicles and Renewable Energies (EVER), Monaco, 2014.